

Joining High Nitrogen Steels with Ag–Cu–Ni Metal Filler



Shuye Zhang, Peng He, Zhenfeng Li, Xingxing Wang, Di Gao,
and Dusan P. Sekulic

Abstract This paper offers a study of a vacuum brazing of high nitrogen steel by using AgCuNi metal filler. Moreover, the precipitation behavior of the second phase of the high nitrogen steel has been analyzed. The result shows that the temperature range of the second phase precipitates has been 700–800 °C. The heat treatment of high nitrogen steel base metal should be avoided in that temperature range. However, it has been established that the heat treatment of the brazing process has little influence on microstructures and mechanical properties of high nitrogen steel, thus, the brazing temperature range was established to be 850–1050 °C. A typical joint microstructure is mainly the Ag–Cu eutectic in the filler layer, and the element diffusion area near the high nitrogen steel side. Brazed joints, with good mechanical properties were obtained at temperatures of 850 °C and 950 °C. It has been established that the optimized brazing process conditions are: (i) the peak temperature of $T = 950$ °C and (ii) the dwell time at the peak of $t = 20$ min. The element diffusion processes of high nitrogen steel brazing have been considered by using molecular dynamics simulations. The diffusion processes of Fe–Cu and Fe–Ni binary systems were simulated. It has been uncovered that in the Fe–Cu diffusion process, only the atoms diffuse mutually. A mesophases were found during the Fe–Ni diffusion process.

Keywords High nitrogen steel · Precipitation in the second phase · Vacuum brazing · Microstructure · Molecular dynamics simulation

S. Zhang (✉) · P. He (✉) · Z. Li · D. Gao
State Key Laboratory of Advanced Welding and Joining, Harbin Institute of Technology, Harbin 150001, China
e-mail: syzhang@hit.edu.cn

P. He
e-mail: hepeng@hit.edu.cn

X. Wang
School of Mechanical Engineering, North China University of Water Resources and Electric Power, Zhengzhou 450045, China

D. P. Sekulic
College of Engineering, University of Kentucky, Lexington 40506, USA

1 Introduction

It is generally accepted that steels with nitrogen content greater than 0.4 wt.% (mass percentage) in the austenitic matrix or nitrogen greater than 0.08 wt.% in the ferritic matrix, are known as high-nitrogen steels (Uggowitzner et al. 1996). In many early applications, scholars used nitrogen to replace nickel so that an austenite structure in steel could be formed (Liu et al. 2020; Vogt 2001; Kaputkina et al. 2016; Petrov et al. 1999). In the austenite, nitrogen is easier to dissolve in a solution than carbon, bringing out a less precipitation of carbides, and consequently a higher strength and corrosion resistance of steel (Qin et al. 2019; Yang et al. 2012; Franks 2015). With the development of the high-nitrogen steel, the researchers have discovered that outstanding properties of such steel, (high strength, good toughness and process performance as well as an excellent corrosion resistance) can be achieved (Li et al. 2015; Hong et al. 2011; Miura and Ogawa 2001; Thyssen and Menné 2010; Simmons 1996). By replacing nickel with nitrogen, the resulting steel features, e.g., good economy with better biocompatibility. The high-nitrogen steel has been widely used in electric power, shipbuilding, marine engineering, military equipment, medical equipment, and other fields (Stein and Hucklenbroich 2004; Kuball et al. 2020; Li et al. 2009; Nishimoto and Mori 2004).

High-nitrogen steel has been adopted as a material for structural components in various equipment structures, requiring a high load-bearing capacity and strong impact resistance. Correspondingly, the fusion welding methods such as laser welding and arc welding have been often used (Zhang et al. 2016; Zhao et al. 2007; Dong et al. 2005; Mohammed et al. 2017). However, in the fields of medical equipment applications, high-nitrogen steel has been used because the load-bearing capacity and impact resistance are not the primary factors to be considered. On the contrary, the corrosion resistance should be put forward as the priority (Baba and Katada 2006; Galloway et al. 2011; Bayoumi and Ghanem 2005). Temperature in the traditional fusion welding is quite near the melting point of the high-nitrogen steel. Nitrogen in a supersaturated solid solution of the austenite has a high risk of N_2 gas formation, which greatly reduces the mechanical performance and corrosion resistance of the joint (Bang et al. 2013; Kuwana 1990; Li et al. 2011). Moreover, the nitrogen gas, which cannot escape in time will form gas voids in the welded joint, thus weaken the mechanical integrity (Geng et al. 2016; Li et al. 2019; Mohammed et al. 2016). Therefore, it is very important to keep the brazing temperature below the melt point of the high-nitrogen steel so that the loss of nitrogen could be avoided (Wang et al. 2021; Zhang et al. 2021; Shi et al. 2018).

This paper studies the brazing process of high-nitrogen austenitic stainless steel. The ultimate objective is to analyze the performance of formed joints. Furthermore, it is important to find the solution for avoiding precipitation of nitrogen during the fusion bonding. The precipitation in the second phase during the brazing process has been considered by using JMAT Pro for thermodynamic calculations. Also, the

brazing holding time and brazing temperature impacts have been analyzed. The influence of joint morphology and technological parameters on the structure and mechanical properties of brazed joints have been studied. Moreover, LAMMPS software was used to conduct the molecular dynamics simulation (Swope et al. 1982; Plimpton 1995; Del Rio et al. 2011; Beeman 1976; Choudhury et al. 2011; Jawalkar et al. 2007) of the high-nitrogen steel matrix elements, such as Fe, Cu and Ni elements. The atomic diffusion process in both the Fe–Cu binary system and the Fe–Ni binary system were simulated to establish whether the intermetallic compounds would be generated. The atomic potential energy was analyzed to obtain the mean square displacement (MSD) and diffusion coefficient to compare the element diffusion ability in the Fe–Cu and Fe–Ni systems.

2 Material and Methods

2.1 The Substrate and Filler Metal

The substrate (base) metal considered is a high-nitrogen austenitic stainless steel with a high nitrogen content of 0.75 wt.%. As shown in Fig. 1, the structure of the base metal is in the forged state of equiaxial grains. The grains are mostly the austenite of uniform sizes including some crystal twinning. The base metal composition of high-nitrogen steel is as shown in Table 1. The filler adopted is Ag–Cu–Ni, in which

Fig. 1 The micro structure of the high-nitrogen austenitic stainless steel

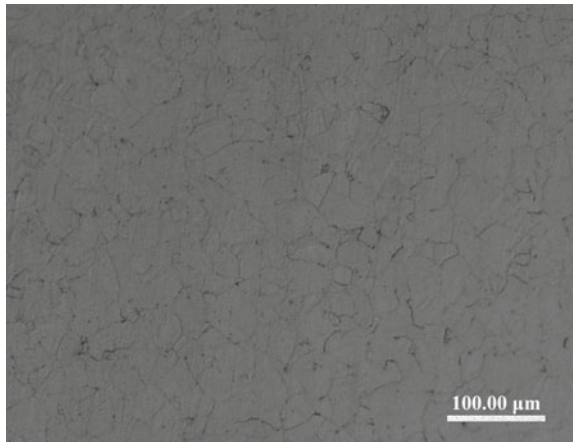


Table 1 The base metal composition of high-nitrogen steel

Element	Cr	Ni	Mo	Mn	Cu	N	C	Fe
wt.%	24	22	8	3	0.5	0.5	≤0.02	Bal

Table 2 The chemical composition of the Ag–Cu–Ni filler

Element	Ag	Cu	Ni
wt. %	71.5	27.75	0.75

0.75% of nickel is added (silver-copper eutectic filler with a particle size of 200 mesh). The chemical composition of the filler is as shown in Table 2.

2.2 Test Equipment and Methods

The M60 vacuum diffusion furnace is adopted as the equipment for the vacuum brazing test. The maximum heating temperature of the vacuum furnace can reach 2150 °C, the effective space of the hot zone is $\Phi 75 \text{ mm} \times 130 \text{ mm}$ and the maximum vacuum $6 \times 10^{-4} \text{ Pa}$. The AgCuNi filler was mixed with ethyl cellulose as a binder to obtain the filler paste. The test specimens were assembled in the form shown in Fig. 2 inset. No pressure was exerted on the assembled specimen during the brazing process.

The process parameters adopted were as follows: the temperature ramp up, to 850 °C, than 950 °C, and ultimately 1050 °C with holding times of 5 min, 10 min, 20 min, respectively, Fig. 2.

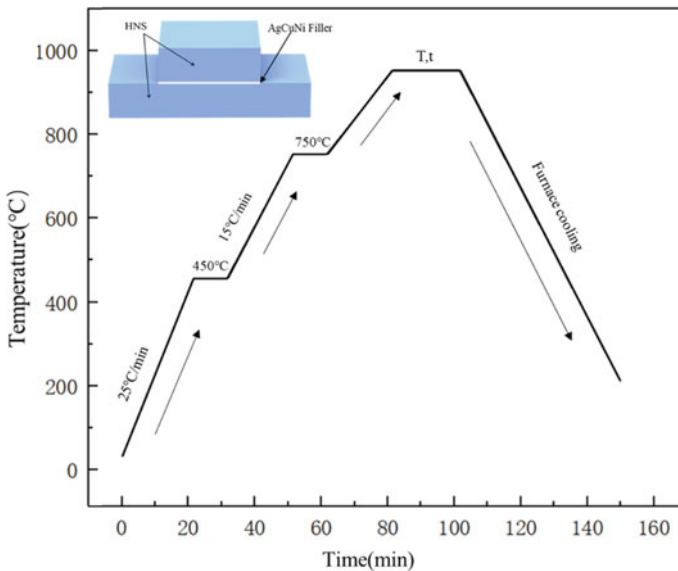


Fig. 2 Brazing process curve

2.3 Microstructure Analysis and Performance Testing

The microstructure of the joint zone was revealed by partitioning the joint with Wire EDM partitioning along the center plane of the joint, and mounted with a dental acrylic resin powder. The samples were polished by sandpaper with 400, 800, 1000, 1200, and 1500 grit, followed by 1 μm diamond polishing agent. An optical microscope was used to conduct optical characterization of the samples. The base metal needs to be corroded to uncover the morphology and the grain boundaries. We chose as an etchant the mixture of 1 ml HF, 1.5 ml HCl, 2.5 ml HNO₃ and 95 ml H₂O. Due to the high corrosion resistance of high-nitrogen steel, the corrosion time will correspondingly last as long as about 100 s. Finally, the corroded base metal and the brazed joints were observed with both metallurgical microscope and scanning electron microscope. The electronic probe was used for the microstructure analysis. The optical microscope (LEICA, DM4500P) and the scanning electron microscope (SEM, Helios Nanolab600i, FEI Company, USA) were used to analyze the microstructure and morphology of the brazed joint interfaces. The energy spectrometers were used for composition analysis.

The shear testing at room temperature has been adopted to evaluate mechanical properties response. The dimensions of the substrates are 10 mm \times 10 mm \times 4 mm and 10 mm \times 20 mm \times 4 mm. The schematic diagram of the shear strength test assembly is shown in Fig. 3. The brazed joint assembly was put into the shear fixture and tested at room temperature, with the shear test speed of 0.5 mm/s. The stress–strain data curve, and the maximum load when the joint was broken were collected during the shear test. The 3 shear tests, under each set of brazing process parameters were collected, and the average value is taken as the average joint strength to ensure the accuracy. The shear strength was measured by a universal tensile testing machine (Instron 5569, Instron Co., USA).

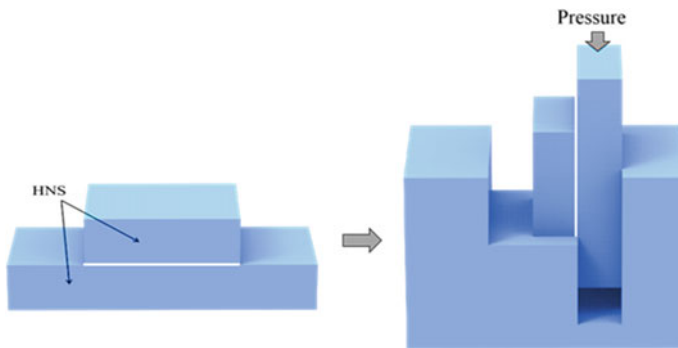


Fig. 3 The schematic diagram of the shear strength test

2.4 Molecular Dynamics Simulation on Element Diffusion Process of Filler and Base Metal

The atomic diffusion simulation of Fe–Cu binary system has been performed by using the NPT ensemble (Berendsen et al. 1984; Martyna et al. 1992; Nosé 1984; Mark et al. 2011; Gervilla et al. 2020). It is assumed that the system is at a constant temperature and pressure. The particle numbers in the system at different brazing temperatures of 850, 950 and 1050 °C have been considered as being constant. For the atomic diffusion simulation in Fe–Ni binary system, we selected the temperatures of 1123, 1223 and 1323 K. No additional pressure is needed during the brazing testing, so a standard atmospheric pressure (0.1 MPa) has been assumed. The diffusion model was constructed with crystalline Fe and crystalline Cu. The lattice constant of Cu atom is 3.61492505 nm and the lattice constant of Fe atom is 2.85532463 nm. For the molecular dynamics model of Fe–Ni diffusion, the lattice constant of Ni atom is 3.506486 nm while the lattice constant of Fe atom is as already adopted, i.e., 2.85532463 nm. For the sake of higher calculation efficiency and appropriately less calculation time, we established the supercells with a smaller number of atoms. About 10 reduplicate unit cells were adopted in the x, y, and z directions, respectively, so as to establish the supercell and keep a small distance between the two crystals. The timestep of the molecular dynamics simulations was 60 fs. The periodic boundary conditions were applied in three directions, and the EAM potential function developed by Bonny et al. (2009, 2013), was adopted to calculate the interatomic force between the Fe and Cu atoms. The potential function including the Fe–Cu–Ni atomic potential was developed by Bonny for the microstructure evolution and mechanical property changes in the steel of reactor pressure vessel as well as the atomic scale diffusion simulation.

3 Results and Discussion

3.1 The Second Phase Precipitation Behavior

The equilibrium phase diagram of high-nitrogen steel calculated by JMAT PRO is shown in Fig. 4. One can observe precipitated phases in a high-nitrogen steel when the temperature rises from 500 °C. The proportion of austenite is close to 60%. As the temperature keeps rising, the austenite content gradually increases and the structure transforms into austenite at 1200 °C, until it's melted at 1380 °C. In the process, the austenite becomes extremely stable without any high temperature δ -ferrite produced. This is mainly because of the high nitrogen and nickel in the high-nitrogen steel. The two elements can stabilize and expand the austenite phase region. This reduces the production of δ -ferrite in the high temperature region and inhibits the martensite phase transformation in the low temperature region.

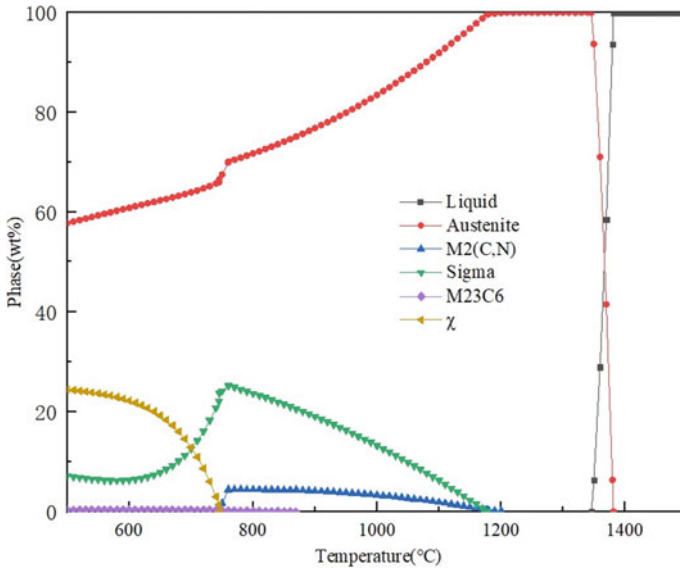


Fig. 4 The equilibrium phase diagram of high-nitrogen steel

In the considered process, the second phase that precipitates in the high-nitrogen steel mainly include M2(C,N) phase, σ phase, M23C6 phase and χ phase. The M2(C,N) phase is mainly the Cr2(C,N) phase, whose precipitation temperature range is about 750–1200 °C; the actual composition of σ phase is $(Fe,Ni)_x(Cr,Mo)_y$. Its precipitation temperature range is relatively large, between 500 and 1200 °C. The peak of precipitation is at 750 °C. The M23C6 phase is mainly the Cr carbide, which has only a small amount of precipitation in the lower temperature range. The chemical composition of χ phase (Chi phase) is mostly $(Fe,Ni)_{36}Cr_{18}Mo_4$ in austenitic steels. The precipitation starts at 750 °C and the proportion of precipitated phases gradually increases as the temperature keeps reducing, which mainly takes place in the low temperature region.

The calculated isothermal cooling transition curve is shown in Fig. 5. The curve can also be regarded as the isothermal precipitation curve to analyze the precipitation time of the precipitated phase when the high-nitrogen steel is held at the corresponding temperature. One can see that the σ phase is the easiest to get precipitated when the heated high-nitrogen steel is cooled, followed by the χ phase and the M2(C,N) phase. For the σ phase, the most sensitive temperature is 780 °C and the incubation period is 4.1 h. For the χ phase, the most sensitive temperature is 750 °C and the incubation period is 6.1 h. For the M2(C,N) phase, the most sensitive temperature is 750 °C and the incubation period is as long as more than 30 h.

Based on the performed analysis, one can assess the sensitive temperature of the second phase precipitation would be 700–800 °C. Therefore, with regard to the brazing process of interest in this paper, the high-nitrogen steel shall not be tested at 700–800 °C.

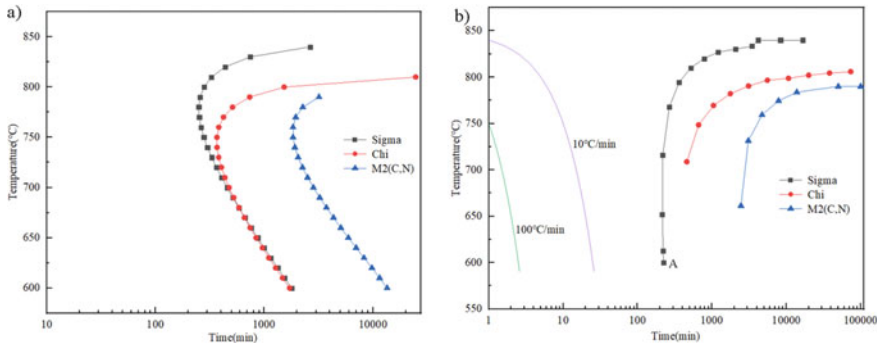


Fig. 5 High nitrogen stainless steel cooling transition curve. **a** Isothermal cooling transition **b** continuous cooling transition

The brazing temperature curve shown in Fig. 2, indicates dwell times of 30 min at 850, 950 and 1050 °C, followed by a convective cool down within the furnace. Polishing and etching followed the tests. The metallographic imaging with the Image-Pro Plus software has been performed to determine the ratio of the precipitated phase. The microstructure result is shown in Fig. 6. It can be seen that continuous precipitates appear at the grain boundaries when the brazing process curve is held at 850 °C for

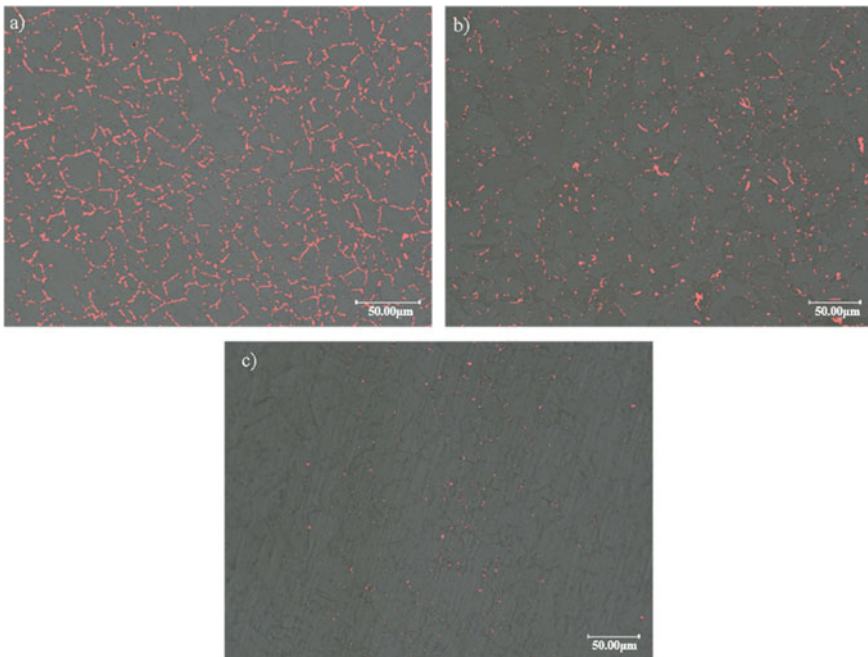


Fig. 6 Microstructure of the joints after the dwell for 30 min. **a** 850 °C, **b** 950 °C, **c** 1050 °C

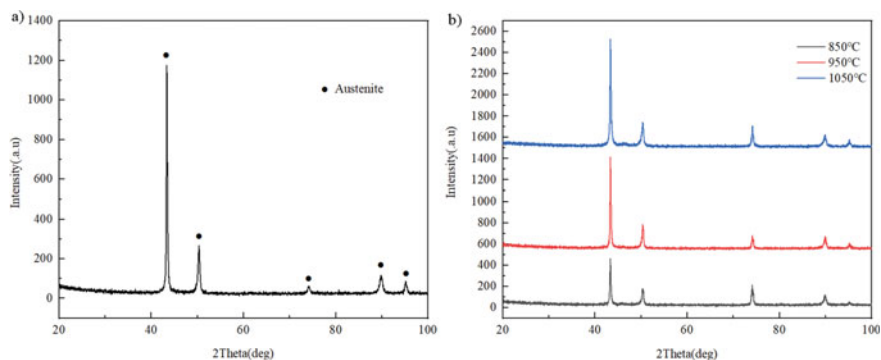


Fig. 7 XRD spectrum line of high-nitrogen steel. **a** Heat dwell at 850 °C, **b** comparison of the three heat treatments

30 min. A small amount of larger granular precipitates appear at the triple grain boundaries. At the holding temperature of 950 °C, a small amount of discontinuous precipitated phases appear on the interface. When the temperature rises to 1050 °C, almost no precipitated phases can be seen within the microstructure.

As the dwell temperature increases, the precipitates in the high-nitrogen steel gradually decrease, which conforms to the result obtained by the thermodynamic calculations. This is because at the higher temperature the deviation from the critical temperature is greater. Since the holding time of brazing is less than 30 min, much shorter than the precipitation incubation time calculated by the phase diagram, less precipitated phase can be observed in the microstructure.

To determine the precipitated phases, XRD analysis is performed. The analysis is performed on the base metal after the aforesaid three heat treatments. The XRD results of base metal after dwell at 850 °C are shown in Fig. 7. By comparing to standard PDF card with Jade software, we find that the diffraction angle is consistent with the diffraction features of austenite standard card, without the diffraction peaks of σ phase and nitride $M_2(C,N)$ phase. The comparison of the three base metals at 850, 950 and 1050 °C, one finds the same diffraction angle for the diffraction peak intensity. Accordingly, we can conclude that the base metals after brazing heating and dwell are still the austenitic structures. There are fewer precipitates, hence the phases with precipitates are not detected.

The brazing dwell and cooling process have little effect on the base metals, consequently such treatments will not produce many precipitates. Therefore, the filler AgCuNi can be used for brazing tests with the temperature range set between 850 and 1050 °C.

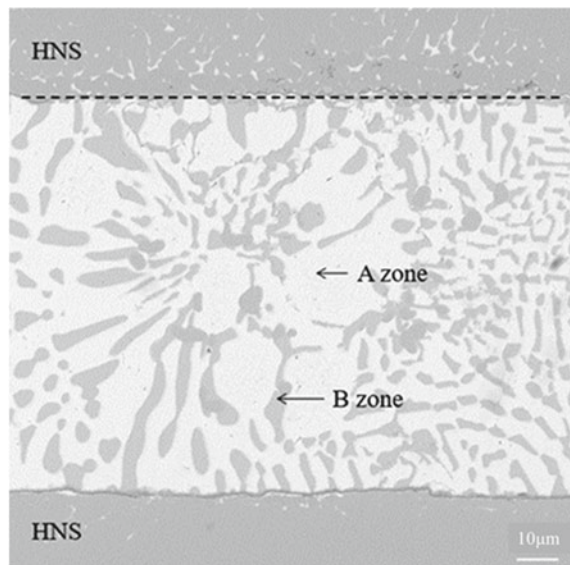
3.2 Microstructure Features of High-Nitrogen Steel Brazed Joint

Analysis is carried out of a typical AgCuNi high-nitrogen steel brazing joint. Under the conditions of the brazing temperature of 850 °C with 20 min of holding time, the obtained microstructure of the joint is shown in Fig. 8. It can be seen that the structure of the joint interface appears to be good, without any defects such as voids and cracks. The joint mainly consists of the Ag–Cu filler layer and the diffusion area beyond the interface between the filler and the base metal. The filler layer is mainly divided into the light-colored area A and the dark-colored area B, according to the contrast difference. The diffusion area mainly includes the high-nitrogen steel base metal and the zone resulting from the filler diffusion into the base metal.

In Fig. 9, it can be seen that the main elements in the filler metal area are Ag, Cu and Ni. These are mostly in the light color area, Ag and a few Cu and Ni, zone A. The B part of the dark regions is mostly Cu, while Ag and Ni constituents are a few. On the base material side of the high nitrogen steel, it is mainly Fe, Cr, Mn and other high nitrogen steel elements.

To determine the reaction products and element diffusion between the filler and the base metal during the brazing process, the interface between the high-nitrogen steel base metal and the filler at brazed joint was highly magnified to obtain the microstructure shown in Fig. 10. Energy Dispersive Spectrometer (EDS) analysis was done on each point shown in the figure and the corresponding chemical composition is shown in Table 3.

Fig. 8 The microstructure of a typical high-nitrogen steel/AgCuNi/ high-nitrogen steel brazed joint, under the brazing temperature of 850 °C and holding time of 20 min



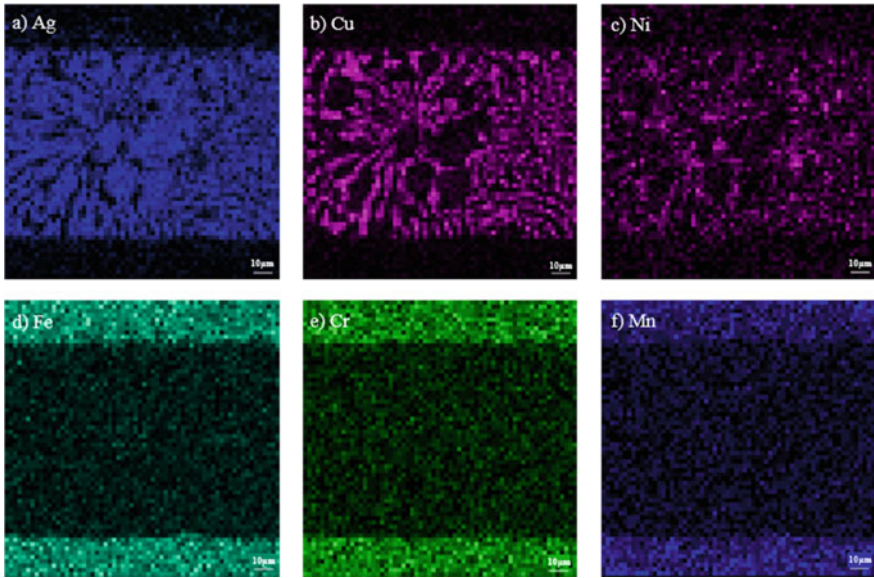


Fig. 9 Surface scan of the main elements on the joint interface. **a** Ag; **b** Cu; **c** Ni; **d** Fe; **e** Cr; **f** Mn

Fig. 10 High power microstructure of brazing joint interface

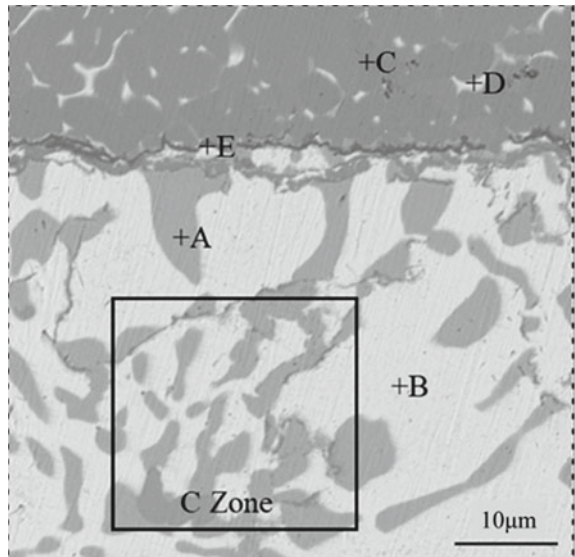


Table 3 Results of energy spectrum analysis (at.%)

	Ag	Cu	Ni	Fe	Cr	Mn	N	Possible phase
A	5.86	73.37	0.96	8.45	3.88	7.47	0	Cu[s,s]
B	68.61	14.13	0.25	3.78	4.74	8.49	0	Ag[s,s]
C	1.93	1.97	1.89	57.77	19.31	12.42	4.71	HNS
D	50.41	5.79	0.82	20.31	8.15	9.72	4.79	Ag/Cu/HNS
E	22.03	6.38	8.03	15.80	6.31	4.73	36.72	AgCu/Ni/M ₂ N

It can be seen from Table 3 that point A and point B in Fig. 10 are Cu-rich phase and Ag-rich phase, respectively. The element at point A is mainly Cu with relatively small amounts of Ag, Fe, Mn and other elements. That means that a small amount of Fe and alloying elements in the base metal diffuse into the filler. Since Cu can dissolve a small amount of alloying elements, point A in the dark-colored area is devised to be the Cu-based solid solution containing a small amount of Ag, Fe and Mn, so it's marked as Cu[s, s]. The element at point B is mainly Ag with a relatively small amount of Cu, Mn and other elements. Point B in the light-colored area is devised to be the Ag-based solid solution containing a relatively small amount of Cu and Mn, so it's marked as Ag[s, s]. The area C shown in Fig. 10 features as the main structure in the middle of the Ag–Cu filler layer. According to the silver-copper phase diagram, it can be seen that the filler composition adopted in this experiment is at the silver-copper eutectic point, so this area is regarded as the Ag–Cu eutectic region. In the filler layer we can find that Mn element concentration has increased compared with other elements of the base metal. That is mainly because the Mn element will dissolve in the AgCuNi filler to increase the wettability and fluidity, which contributes to further wetting and spreading of the filler. The element at point C is mainly Fe as well as a small amount of Cr–Mn alloying element and N. The atomic percentage of nitrogen is 4.71% and the mass percentage is 1.21%. The overall element ratio is close to that of high-nitrogen steel, so this area is mainly the high-nitrogen steel base metal. The element at point D is mainly Ag as well as Fe, Cr, Mn and other elements with the composition ratio close to that of base metal. Therefore, it is devised to be the area formed by the diffusion of filler in high-nitrogen steel base metal. Point E is at the interface between filler layer and base metal with complicated element structure. Apart from Ag, Cu and other elements of high-nitrogen steel, there are also a large amount of N element and an enrichment of Ni. During the brazing process, Ni in the Ni-containing filler forms a transition layer at the interface between filler and base metal thus making a better bonding with an effectively improved corrosion resistance (Baskes and Daw 1984; Chang et al. 2020). With regard to a large amount of N, it is supposed that during the brazing and heat-preservation process, N in the high-nitrogen steel base metal has stronger diffusivity, while diffusing along the direction of grain boundaries and the interface. After being aggregated at the interface, it precipitates in the form of nitrides with Fe, Cr, Mn and other elements.

To sum up, in the structure of high-nitrogen steel brazing joint, the Ag and Cu will hardly react with the alloy elements in the high-nitrogen steel without producing a new intermetallic compound reaction layer. However, the Ag–Cu filler and high-nitrogen steel base metal diffuse with each other to form the diffusion area at the joint. A small amount of Cu, Mn and other elements are dissolved in Ag in the middle of the joint zone to form the Ag-based solid solution, in which the Ag–Cu eutectic structure is distributed. The Ni, N element enrichment areas are at the interface of base metal and filler. Ag and Cu elements diffuse on the base metal side to form a white striped mixed area. Therefore, the typical joints can be divided into the zones as follows: (1) the filler layer, that is, the Ag-based solid solution and the Ag–Cu eutectic structure in the middle of the joint; (2) Ni, N element enrichment area at the transition layer of the interface between base metal and filler; (3) diffusion area on the side of high-nitrogen steel base metal.

3.3 Molecular Dynamics Analysis

3.3.1 Fe–Cu and Fe–Ni Diffusion Process

The simulation shown in Fig. 11 is the result of the calculation of Fe–Cu atom diffusion model at the times of 0 ps, 200 ps, 400 ps and 600 ps at the temperature of 1123 K (850 °C). One can see that when the diffusion gets started, the gap between Fe and Cu atoms disappears. The right side of atom distribution diagram shows the concentration distributions of Fe and Cu atoms along the Z axis in the diffusion direction, (the interface is located at 30 nm on the Z axis). By comparing the four atomic diffusion models and atomic concentration distribution diagrams at different periods of time, we can see that as the time goes by, the thickness of diffusion area gradually increases and the Fe atoms start to diffuse into the Cu lattice. The Fe atoms on the side of the Cu lattice start to increase, although only a small number of Cu atoms diffuse into the Fe lattice. During the diffusion process, the thickness of diffusion area increases as the diffusion time goes by. Note that the concentration curve of the Fe–Cu diffusion system is basically the linear one, which means that species diffuse in the holding process mutually without a mesophase compound generated. Such a result conforms to the ultimate mutual solubility in Fe–Cu binary phase diagram without the mesophase generated.

The diagram shown in Fig. 12 is the model of Fe–Ni atom diffusion at the time instances of 0 ps, 200 ps, 400 ps and 600 ps. The temperatures was 1123 K (850 °C). We can see that when the diffusion gets started, the gap between Fe and Ni atoms disappears immediately. The subsequent diffusion and migration processes can be observed. Similar to the Fe–Cu diffusion, the right side, see Fig. 12, shows the atom concentration distribution along the diffusion direction. The interface is located at the distance of 30 nm. The thickness of diffusion area gradually increases as the diffusion time evolves. The Fe–Ni atom diffusion is also known as the asymmetric. More Fe atoms diffuse into the Ni lattice while only a small number of Ni atoms

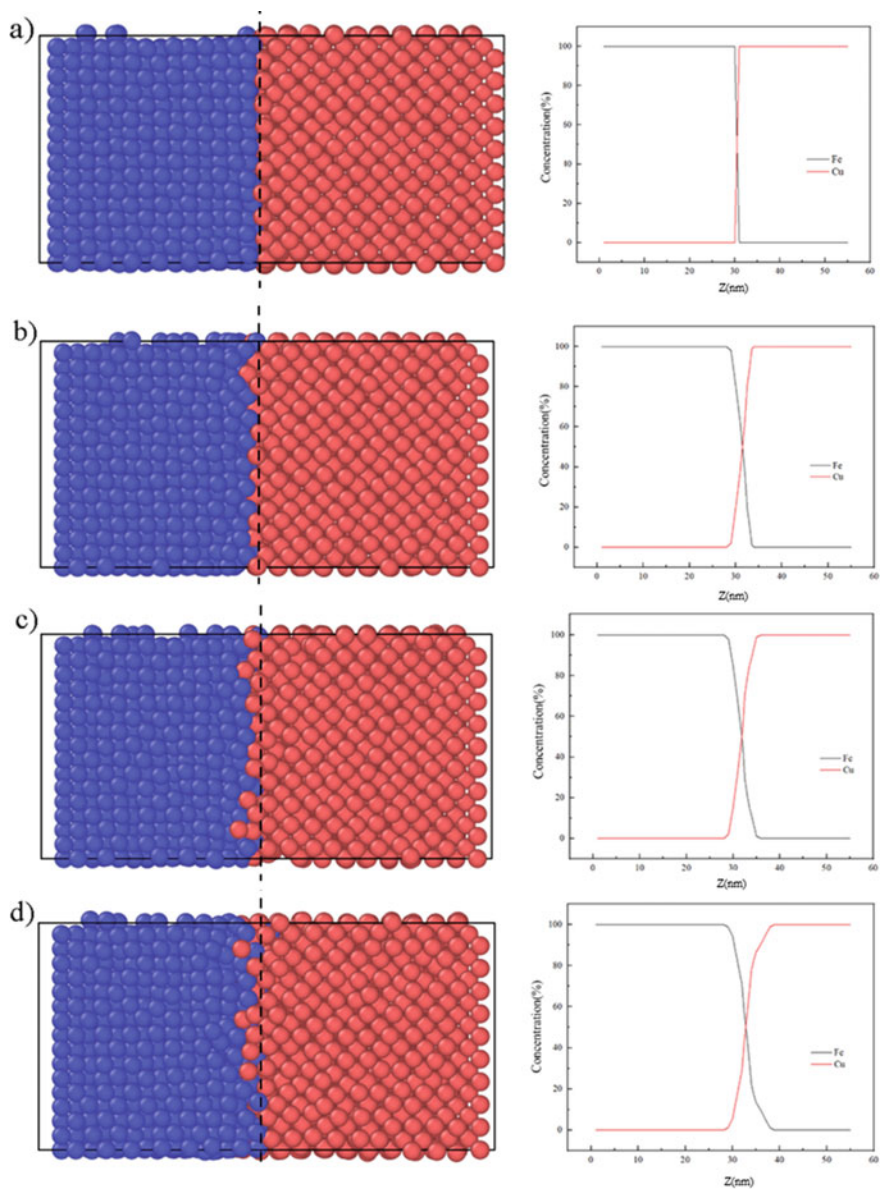


Fig. 11 The atomic distribution diagram and the concentration diagram along Z axis of Fe-Cu for different diffusion time (850 °C): **a** 0 ps; **b** 200 ps; **c** 400 ps; **d** 600 ps

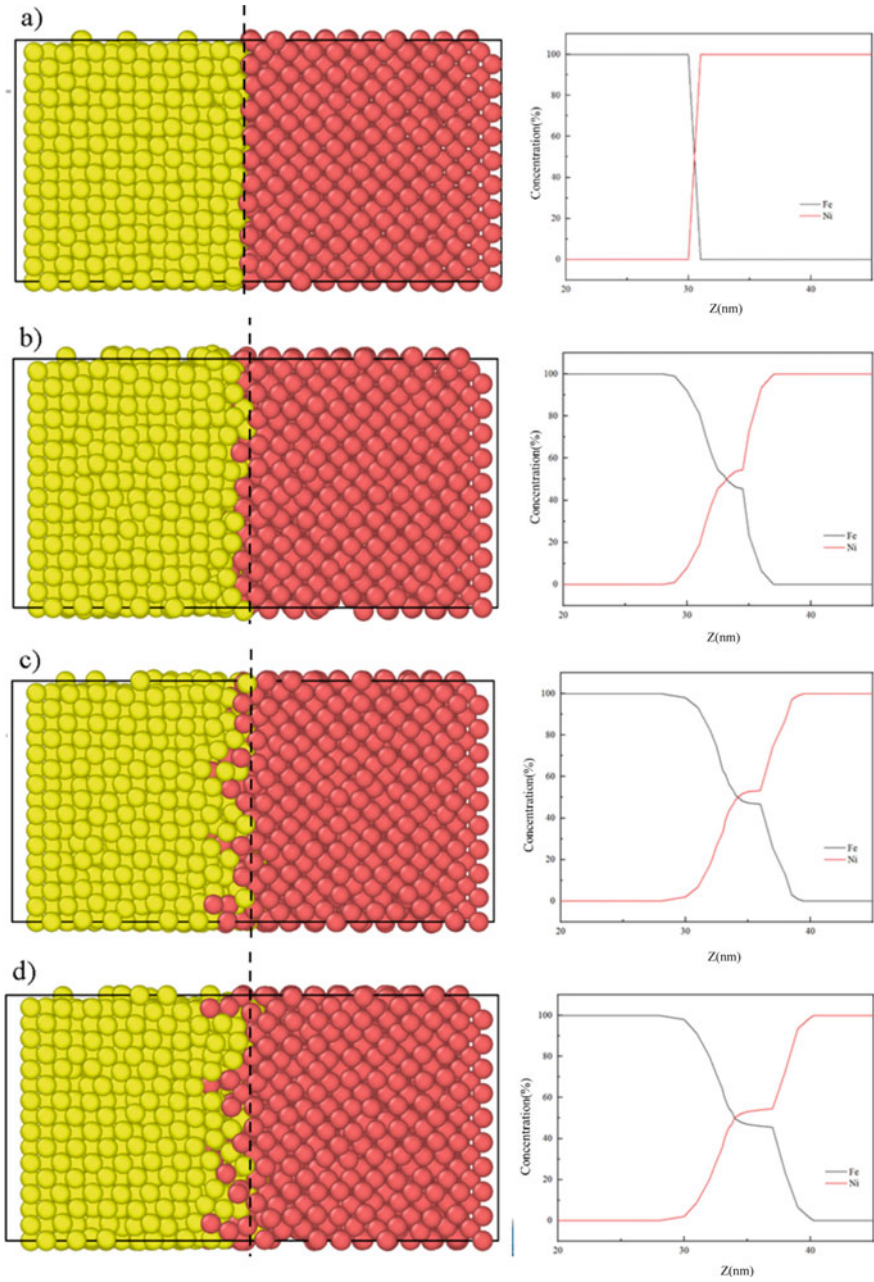


Fig. 12 The atomic distribution diagram and concentration diagram along Z axis of Fe–Ni with different diffusion time (850°C): **a** 0 ps; **b** 200 ps; **c** 400 ps; **d** 600 ps

diffuse into the Fe lattice. It can be inferred that the diffusion ability of Fe atoms is stronger than that of Ni atoms in the Fe–Ni binary system.

Compared to the diffusion in the Fe–Cu binary system, the diffusion area of Fe–Ni system is thicker, with more obvious diffusion under the same time and temperature conditions. Moreover, compared to the Fe–Cu diffusion system, the concentration curve of Fe–Ni system shows a section with a smaller slope in the diffusion domain. A mesophase is formed in this domain during the diffusion process, which means a certain amount of Fe–Ni compound is generated (Ouyang et al. 2018). By referring to the Fe–Ni binary phase diagram, it can be seen that some mesophase including FeNi, and FeNi₃ had been generated between Fe and Ni. This is consistent with the conclusion of the molecular dynamic simulation.

3.3.2 Atomic Potential Energy in Diffusion Process

At the diffusion time of 600 ps and at three different temperatures, we have compared the atomic potential energy in the considered Fe–Cu diffusion process. The result is shown in Fig. 13. The potential energy of an atom is zero in the equilibrium position. When the atom is away from the equilibrium position, the potential energy changes to a negative value. The smaller distance between atoms, the greater deviation from the equilibrium position and the greater absolute value of atomic potential energy. It can be seen from the figure that in the diffusion process, the absolute potential energy value of Fe atoms is greater than that of Cu atoms. This means that the Fe atoms are further away from the equilibrium position and thus become more unstable. By averaging the atomic potential energy of Fe and Cu at the considered three temperatures, one gets the results are shown in Table 4. For the same Fe or Cu atoms, the absolute value of the atomic potential energy increases as the temperature increases, and the atoms become more unstable and easier to break the barrier to get diffused.

Similarly, we have calculated the potential energy of each atom in the diffusion process based on a molecular dynamics simulation. At the diffusion time of 600 ps and at the three temperatures, we have compared the atomic potential energy in Fe–Ni diffusion process. The result is shown in Fig. 14. It can be seen that during the diffusion process, the absolute potential energy value of Fe atoms is smaller than that of Ni atoms. This means that the atoms start to move away from the equilibrium positions. Moreover, the Ni atoms get further away from the equilibrium position and become more unstable. By averaging the atomic potential energy of Fe and Ni at three temperatures, one obtains the results are shown in Table 5. For the same Fe or Ni atoms, the result of atomic potential energy appears to be the same as that obtained in the Fe–Cu diffusion simulation. As the temperature increases, the absolute value of atomic potential energy increases and the atoms become more unstable and easier to break the barrier, hence to get diffused.

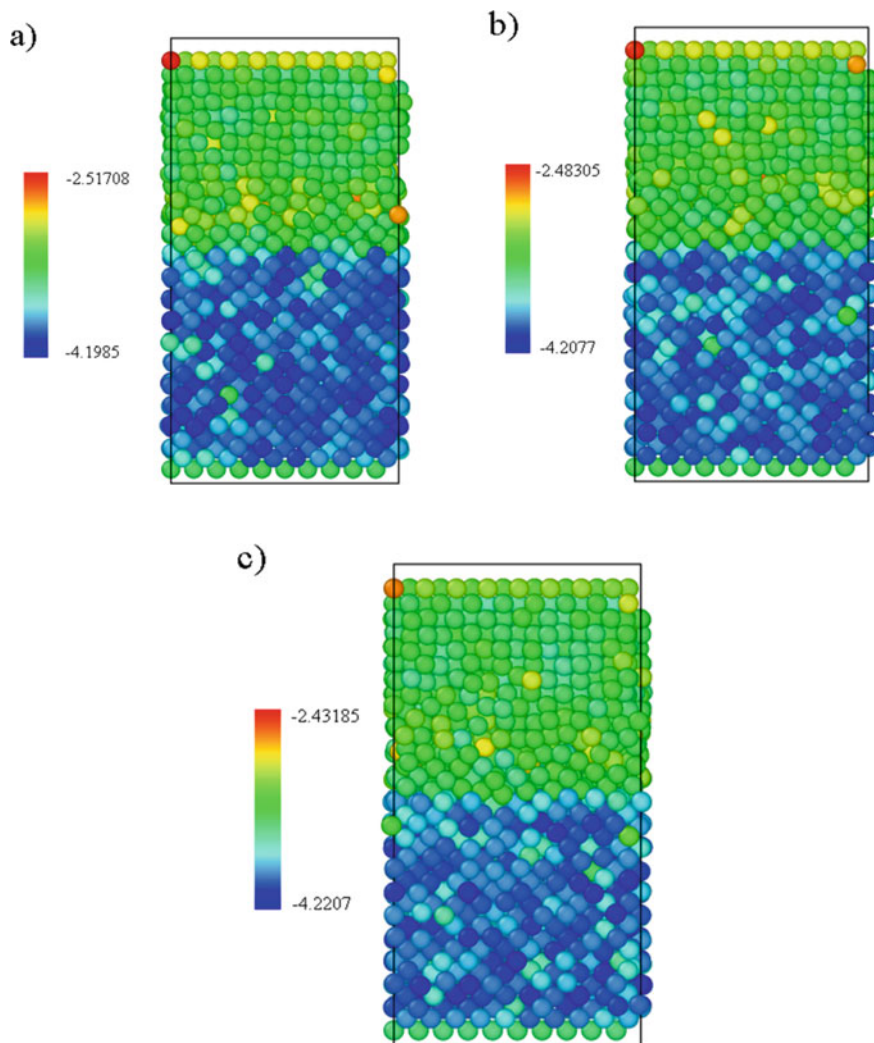


Fig. 13 Diagram of Fe–Cu atomic potential energy at 600 ps and the three different temperatures; **a** 1123 K; **b** 1223 K; **c** 1323 K

Table 4 Average potential energy of Fe and Cu atoms at different temperatures

Temperature	1123 K	1223 K	1323 K
Fe	–3.8522 eV	–3.8717 eV	–3.8829 eV
Cu	–3.2708 eV	–3.2881 eV	–3.2975 eV

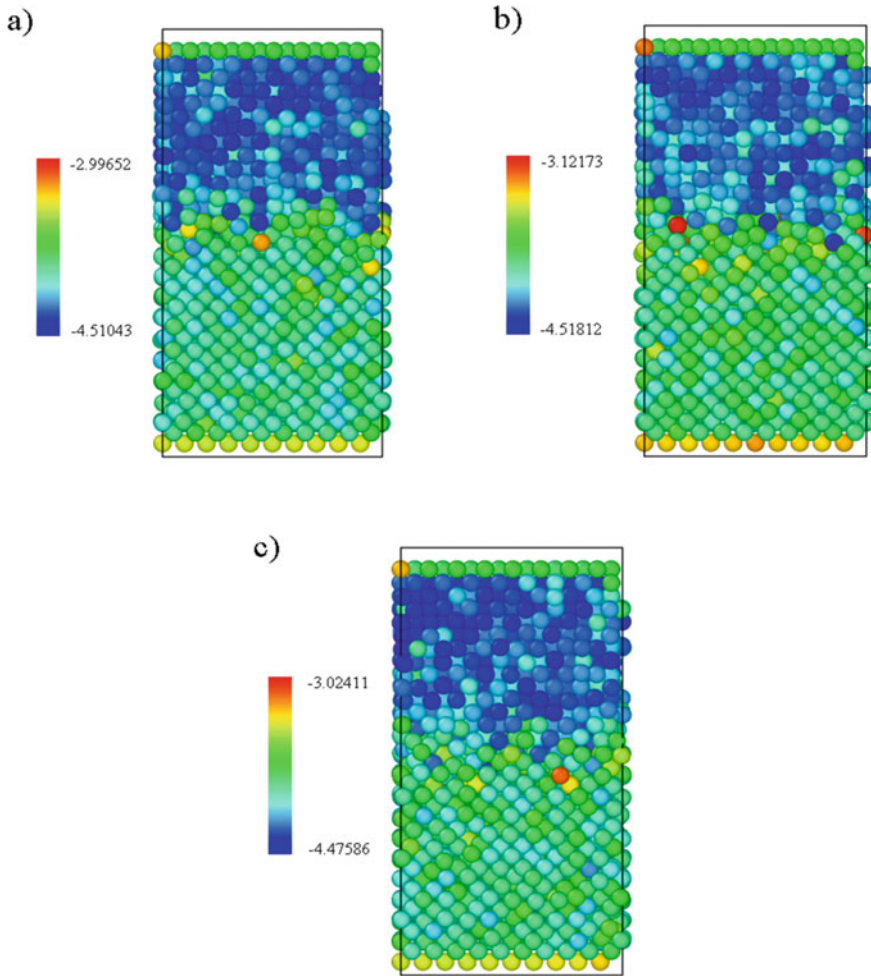


Fig. 14 Diagram of Fe–Ni atomic potential energy at 600 ps in different temperatures; **a** 1123 K, **b** 1223 K, **c** 1323 K

Table 5 Average potential energy of Fe and Ni atoms at different temperatures

Temperature	1123 K	1223 K	1323 K
Fe	−3.8532 eV	−3.8731 eV	−3.8847 eV
Ni	−4.1838 eV	−4.1985 eV	−4.2066 eV

3.3.3 Diffusion Coefficient

The Mean Square Displacement (MSD) evaluations indicate different diffusion ability of Fe and Cu atoms as well as the Fe and N atoms, Tables 6 and 7. These data

Table 6 Comparison of the MSD of Fe and Cu in different time at 1323 K

Time (ps)	60	180	300	480	600
MSD of Fe (10^{-9}m^2)	3.27739	5.33243	7.77702	11.4883	14.9785
MSD of Cu (10^{-9}m^2)	2.56587	4.73497	7.03857	10.8754	13.7495

Table 7 Comparison of the MSD of Fe and Ni in different time at 1323 K

Time (ps)	60	180	300	480	600
MSD of Fe (10^{-9}m^2)	2.60847	3.16528	3.87163	5.36935	6.3628
MSD of Ni (10^{-9}m^2)	2.46461	4.73497	3.64864	5.04519	5.9719

can be used to calculate the diffusion coefficient.

The MSD comparison of Fe and Cu atoms is shown in Table 6, from which we can see that at the given temperature, the MSD of Fe atoms is generally higher than that of Cu atoms. Therefore, we can infer that the diffusion ability of Fe atoms is greater than that of Cu atoms in the Fe–Cu binary diffusion system.

Similarly, the MSD of Fe atoms and Ni atoms increases linearly as the diffusion process continues. The MSD comparison of Fe and Ni atoms is shown in Table 7, from which we can see that at the given temperature, the MSD of Fe atoms is generally higher than that of Ni atoms. Therefore, we can infer that the diffusion ability of Fe atoms is greater than that of Ni atoms in the Fe–Ni binary diffusion system.

4 Conclusions

In this study, high nitrogen steel was bonded by a vacuum brazing process with AgCuNi as a filler braze. The second phase precipitation of high nitrogen steel under brazing process was empirically and numerically considered. Typical interface morphology of the joints was analyzed. Moreover, we have discussed the influence of different technological parameters on the joint interface structure and mechanical properties. The specific results of this study can be summarized as follows:

- (1) The second phase precipitation behavior of high nitrogen steel exposed to a brazing process has been analyzed. The phase diagram and cooling transition curve of high nitrogen steel have been obtained through a thermodynamic calculation. A conclusion has been reached that the critical temperature range for the second phase precipitates is 700°C – 800°C . Therefore, the brazing process should be avoided in that temperature range. The calculation illustrates that the cooling process has little significance for the cooling speed, and the second phase can be avoided during the furnace. We have established that the heat treatment of the brazing process studied had a little influence on the

high nitrogen steel. The brazing temperature range was determined to be 850 °C–1050 °C.

- (2) The brazing heating and cooling treatment impact on the high nitrogen steel was studied. Furthermore, the precipitation of the second phase in the high nitrogen steel has been considered. Because the critical temperature range is avoided and the brazing holding time is shorter than the “incubation period” of the precipitated phase, so the precipitation is reduced. The composition of the precipitated phase cannot be determined by XRD.
- (3) The brazing process is dominantly characterized by diffusion between the migrating elements. Typical joint structure is mainly the Ag–Cu eutectic of the filler layer with the element diffusion domain on the substrate material side. Typical joints domains can be divided into the areas as follows: (1) the filler layer, that is, the Ag-based solid solution and the Ag–Cu eutectic structure in the middle of the resolidified braze; (2) Ni and N enrichment area within the transition layer of the interface between the substrate (base) metal and filler; (3) elements diffusion area on the side of the high-nitrogen steel base metal.
- (4) A simulation of molecular dynamics diffusion was conducted on the Fe–Cu and Fe–Ni binary systems respectively and obvious mutual diffusion phenomena were found. The thickness of the diffusion layer has increased with the diffusion time. However, according to the distribution curve of atomic concentration, one can see that there is only a mutual diffusion process in the Fe–Cu binary system while in the Fe–Ni binary system there are both a diffusion process and a generation of the Fe–Ni compound mesophase. According to the calculation and analysis of (i) the element diffusion MSD and (ii) the diffusion coefficient in the two systems at different temperatures, one can see that the higher temperature, the greater is atom MSD and the diffusion coefficient, with a stronger diffusion capacity.

Acknowledgements The authors acknowledge the Natural Science Foundation Excellent Youth Project of Henan (Grant number: 202300410268), and the China Postdoctoral Science Foundation (Project number: 2019M651280, 2019M662011), Open Fund of State Key Laboratory of Advanced Brazing Filler Metals and Technology (Project number: SKLABFMT201901).

Conflicts of Interest

The authors declare that they have no conflict of interest.

Data Availability Statement

The raw/processed data required to reproduce these findings cannot be shared at this time due to technical limitations.

References

- Baba, H., Katada, Y.: Effect of nitrogen on crevice corrosion in austenitic stainless steel. *Corros. Sci.* **48**(9), 2510–2524 (2006)

- Bang, K., Pak, S., Ahn, S.: Evaluation of weld metal hot cracking susceptibility in superaustenitic stainless steel. *Met. Mater. Int.* **19**(6), 1267–1273 (2013)
- Baskes, M.I., Daw, M.S.: Embedded-atom method: Derivation and application to impurities, surfaces, and other defects in metals. *Phys. Rev. B* **29**(12), 6443–6453 (1984)
- Bayoumi, F.M., Ghanem, W.A.: Effect of nitrogen on the corrosion behavior of austenitic stainless steel in chloride solutions. *Mater. Lett.* **59**(26), 3311–3314 (2005)
- Beeman, D.: Some multistep methods for use in molecular dynamics calculations. *J. Comput. Phys.* **20**(2), 130–139 (1976)
- Berendsen, H.J.C., Postma, J.P.M., Van Gunsteren, W.F., DiNola, A., Haak, J.R.: Molecular dynamics with coupling to an external bath. *J. Chem. Phys.* **81**(8), 3684–3690 (1984)
- Bonny, G., Pasionot, R.C., Castin, N., Malerba, L.: Ternary Fe–Cu–Ni many-body potential to model reactor pressure vessel steels: first validation by simulated thermal annealing. *Philos. Mag.* **89**(34–36), 3531–3546 (2009)
- Bonny, G., Castin, N., Terentyev, D.: Interatomic potential for studying ageing under irradiation in stainless steels: the FeNiCr model alloy. *Model Simul. Mater. Sci.* **21**(8), 85004 (2013)
- Choudhury, S., Barnard, L., Tucker, J.D., Allen, T.R., Wirth, B.D., Asta, M., Morgan, D.: Ab-initio based modeling of diffusion in dilute bcc Fe–Ni and Fe–Cr alloys and implications for radiation induced segregation. *J. Nucl. Mater.* **411**(1), 1–14 (2011)
- Del Rio, E., Sampedro, J.M., Dogo, H., Caturla, M.J., Caro, M., Caro, A., Perlado, J.M.: Formation energy of vacancies in FeCr alloys: dependence on Cr concentration. *J. Nucl. Mater.* **408**(1), 18–24 (2011)
- Dong, W., Kokawa, H., Sato, Y.S., Tsukamoto, S.: Nitrogen desorption by high-nitrogen steel weld metal during CO₂ laser welding. *Metall. Mater. Trans. B* **36**(5), 677–681 (2005)
- Franks, R.: Tension and compression stress-strain characteristics of cold-rolled austenitic chromium-nickel and chromium-manganese-nickel stainless steels. *J. Aeronaut. Sci.* **9**(11), 419–438 (2015)
- Galloway, A., McPherson, N., Baker, T.: An evaluation of weld metal nitrogen retention and properties in 316LN austenitic stainless steel. *Proc. Inst. Mech. Eng. Part L J. Mater. Design Appl.* **225**, 61–69 (2011)
- Geng, X., Feng, H., Jiang, Z., Li, H., Zhang, B., Shucai, Z., Wang, Q., Li, J.: Microstructure, mechanical and corrosion properties of friction stir welding high nitrogen martensitic stainless steel 30Cr15Mo1N. *Metals Basel* **6**, 301 (2016)
- Gervilla, V., Zarshenas, M., Sangiovanni, D.G., Sarakinos, K.: Anomalous versus normal room-temperature diffusion of metal adatoms on graphene. *J. Phys. Chem. Lett.* **11**(21), 8930–8936 (2020)
- Hong, C., Shi, J., Sheng, L., Cao, W., Hui, W., Dong, H.: Influence of hot working on microstructure and mechanical behavior of high nitrogen stainless steel. *J. Mater. Sci.* **46**(15), 5097–5103 (2011)
- Jawalkar, S.S., Raju Halligudi, S.B., Sairam, M., Aminabhavi, T.M.: Molecular modeling simulations to predict compatibility of poly (vinyl alcohol) and chitosan blends: A comparison with experiments. *J. Phys. Chem. B* **111**(10), 2431–2439 (2007)
- Jinbao, C., Yingli, Z., Shuang, J.: Effect of solution treatment and aging on microstructure of low-nickel high nitrogen austenitic stainless steel. *Heat Treat. Met.* **45**(02), 120–124 (2020)
- Kaputkina, L.M., Svyazhin, A.G., Smarygina, I.V., Bobkov, T.V.: Corrosion resistance of high-strength austenitic chromium–nickel–manganese steel containing nitrogen. *Steel Translation* **46**(9), 644–650 (2016)
- Kuball, C.M., Jung, R., Uhe, B., Meschut, G., Merklein, M.: Influence of the process temperature on the forming behaviour and the friction during bulk forming of high nitrogen steel. *J. Adv. Joining Process.* **1**, 100023 (2020)
- Kuwana, T.: *The Oxygen and Nitrogen Absorption of Iron Weld Metal During Arc Welding*, pp. 117–128. Springer Netherlands (1990)
- Li, H., Jiang, Z., Cao, Y., Zhang, Z.: Fabrication of high nitrogen austenitic stainless steels with excellent mechanical and pitting corrosion properties. *Int. J. Miner. Metall. Mater.* **16**, 387–392 (2009)

- Li, H.B., Jiang, Z.H., Ma, Q.F., Li, W.M.: Manufacturing high nitrogen austenitic stainless steels by pressurized induction furnace. *Appl. Mech. Mater.* **52–54**, 1687–1691 (2011)
- Li, H.B., Jiang, Z.H., Feng, H., Zhang, S.C., Li, L., Han, P.D., Misra, R.D.K., Li, J.Z.: Microstructure, mechanical and corrosion properties of friction stir welded high nitrogen nickel-free austenitic stainless steel. *Mater. Design* **84**, 291–299 (2015)
- Li, J., Li, H., Peng, W., Xiang, T., Xu, Z., Yang, J.: Effect of simulated welding thermal cycles on microstructure and mechanical properties of coarse-grain heat-affected zone of high nitrogen austenitic stainless steel. *Mater. Char.* **149**, 206–217 (2019)
- Liu, Z., Fan, C., Chen, C., Ming, Z., Wang, L.: Optimization of the microstructure and mechanical properties of the high nitrogen stainless steel weld by adding nitrides to the molten pool. *J. Manuf. Process* **49**, 355–364 (2020)
- Mark, P., Zhang, Q., Czjzek, M., Brumer, H., Ågren, H.: Molecular dynamics simulations of a branched tetradecasaccharide substrate in the active site of a xyloglucan endo-transglycosylase. *Mol. Simulat.* **37**(12), 1001–1013 (2011)
- Martyna, G.J., Klein, M.L., Tuckerman, M.: Nosé-Hoover chains: the canonical ensemble via continuous dynamics. *J. Chem. Phys.* **97**(4), 2635–2643 (1992)
- Miura, H., Ogawa, H.: Preparation of nanocrystalline high-nitrogen stainless steel powders by mechanical alloying and their hot compaction. *Mater. Trans.* **42**(11), 2368–2373 (2001)
- Mohammed, R., Reddy, G.M., Rao, K.S.: Effect of filler wire composition on microstructure and pitting corrosion of nickel free high nitrogen stainless steel gta welds. *T. Indian I. Metals* **69**(10), 1919–1927 (2016)
- Mohammed, R., Madhusudhan Reddy, G., Srinivasa Rao, K.: Welding of nickel free high nitrogen stainless steel: Microstructure and mechanical properties. *Defence Technol.* **13**(2), 59–71 (2017)
- Nishimoto, K., Mori, H.: Hot cracking susceptibility in laser weld metal of high nitrogen stainless steels. *Sci. Technol. Adv. Mat.* **5**(1), 231–240 (2004)
- Nosé, S.: A molecular dynamics method for simulations in the canonical ensemble. *Mol. Phys.* **52**(2), 255–268 (1984)
- Ouyang, Y., Wu, J., Zheng, M., Chen, H., Tao, X., Du, Y., Peng, Q.: An interatomic potential for simulation of defects and phase change of zirconium. *Comp. Mater. Sci.* **147**, 7–17 (2018)
- Petrov, Y.N., Gavriljuk, V.G., Berns, H., Escher, C.: Nitrogen partitioning between matrix, grain boundaries and precipitates in high-alloyed austenitic steels. *Scripta Mater.* **40**(40), 669–674 (1999)
- Plimpton, S.: Fast parallel algorithms for short-range molecular dynamics. *J. Comput. Phys.* **117**(1), 1–19 (1995)
- Qin, Y., Li, J., Herbig, M.: Microstructural origin of the outstanding durability of the high nitrogen bearing steel X30CrMoN15–1. *Mater. Char.* **159**, 110049 (2019)
- Shi, H., Yu, Z., Cho, J.: A study on the microstructure and properties of brazing joint for Cr18-Ni8 steel using a BNi7+9%Cu mixed filler metal. *Vacuum* **151**, 226–232 (2018)
- Simmons, J.W.: Overview: high-nitrogen alloying of stainless steels. *Mater. Sci. Eng., A* **207**(2), 159–169 (1996)
- Stein, G., Hucklenbroich, I.: Manufacturing and applications of high nitrogen steels. *Mater. Manuf. Process.* **19**(1), 7–17 (2004)
- Swope, W.C., Andersen, H.C., Berens, P.H., Wilson, K.R.: A computer simulation method for the calculation of equilibrium constants for the formation of physical clusters of molecules: application to small water clusters. *J. Chem. Phys.* **76**(1), 637–649 (1982)
- Thyssen, J.P., Menné, T.: Metal allergy—a review on exposures, penetration, genetics, prevalence, and clinical implications. *Chem. Res. Toxicol.* **23**(2), 309–318 (2010)
- Uggowitzer, P., Magdowski, R., Speidel, M.: Nickel free high nitrogen austenitic steels. *Isij. Int.* **36**, 901–908 (1996)
- Vogt, J.B.: Fatigue properties of high nitrogen steels. *J. Mater. Process. Tech.* **117**(3), 364–369 (2001)

- Wang, Q., Zhang, S., Lin, T., Zhang, P., He, P., Paik, K.: Highly mechanical and high-temperature properties of Cu–Cu joints using citrate-coated nanosized Ag paste in air. *Progress Nat. Sci. Mater. Int.* **31**(1), 129–140 (2021)
- Yang, K., Ren, Y., Wan, P.: High nitrogen nickel-free austenitic stainless steel: a promising coronary stent material. *Sci. China Technol. Sci.* **55**(2), 329–340 (2012)
- Zhang, H., Wang, D., Xue, P., Wu, L.H., Ni, D.R., Ma, Z.Y.: Microstructural evolution and pitting corrosion behavior of friction stir welded joint of high nitrogen stainless steel. *Mater. Design* **110**, 802–810 (2016)
- Zhang, S., Wang, Q., Lin, T., Zhang, P., He, P., Paik, K.: Cu–Cu joining using citrate coated ultra-small nano-silver pastes. *J. Manuf. Process* **62**, 546–554 (2021)
- Zhao, L., Tian, Z., Peng, Y.: Porosity and nitrogen content of weld metal in laser welding of high nitrogen austenitic stainless steel. *Isij Int.* **47**(12), 1772–1775 (2007)